An Extended Eddy-Preserving Scheme for Draft Tube Flows

Liu Yang[*]
Department of Mechanical Engineering
McGill University
Montreal, Quebec, H3A 0C3, Canada
Email address:
liu.yang4@mail.mcgill.ca

Yao Jiang
Department of Mechanical Engineering
McGill University
Montreal, Quebec, H3A 0C3, Canada
Email address:
yao.jiang@mail.mcgill.ca

Siva Nadarajah[†]
Associate Professor
Department of Mechanical Engineering
McGill University
Montreal, Quebec, H3A 0C3, Canada
Email address: siva.nadarajah@mcgill.ca

The eddy-preserving limiter has been demonstrated to outperform the conventional van Albada limiter for Monotone Upstream-centered Schemes for Conservation Laws (MUSCL) for vortical flows. It reduces the dissipation by inactivating the conventional van Albada limiter in the interpolation of velocity components on the swirl plane of the vortex. In this work, we extend the limiter for the interpolation of pressure, since a minimum pressure often exists along the axis of a free vortex. Three-dimensional vortex advection cases are employed to demonstrate the effects of the novel scheme. An extended eddy-preserving limiter scheme has been demonstrated to further improve the preservation of the pressure extrema. Finally, the scheme is applied to flow through a draft tube (BulbT test case) and the numerical results are compared against experimental data.

Nomenclature

c speed of sound
p pressure
y^+ dimensionless wall distance
M local Mach number
M_{ref} reference Mach number
$\mathbf{P}$ preconditioning matrix
$\mathbf{R}$ vector of residuals
$\mathbf{S}_0$ Cartesian coordinate system
$\mathbf{S}_\omega$ vortex coordinate system
$\mathbf{V}$ vector of primitive variables
$\mathbf{v}$ vector of velocity

$\mathbf{W}$ vector of conservative variables
$\mathbf{W}_0$ vector of entropy variables
α dissipation scaledown factor
σ eigenvalues of the velocity gradient tensor
ρ density
Φ slope limiter
χ recovery coefficient

1   Introduction

Hydroelectricity is a source of renewable energy with numerous favourable features: safe, clean, highly efficient, low-cost, and flexible. However, the deregulation of electricity markets and the integration of wind power brought important changes to the operating patterns of hydro units. Hydro turbines have to operate at off-design conditions to adapt to the demands of the grid. At off-design operating conditions, the reliability and safety of the hydro turbines are challenged by the unsteady complex flow. Accurate numerical simulations with validation against experiments must be conducted to better understand the flow phenomenon and thus prevent the potential risks.

The draft tube is an important component of a hydro turbine. The role of the draft tube is to decelerate the flow from the turbine runner and convert its dynamic pressure into a rise of static pressure [1]. At part load conditions, the energy is not fully utilized by the runner-shaft-rotor, resulting in high residual swirl when the flow exits the runner. The swirling flow with high angular momentum enters the draft tube and encounters the lower momentum fluid in the inlet conical zone. The shear layer between them gives rise to a large helical precessing vortex, commonly referred to as a vortex

---

[*]Address all correspondence related to ASME style format and figures to this author.

[†]Address all correspondence for other issues to this author.

rope. Due to the adverse pressure gradient and hydraulic instabilities present in the draft tube, the vortex breaks down and a reverse flow occurs, further complicating the flow phenomena. As a consequence, at part load conditions, the turbine experiences severe low frequency and large amplitude pressure fluctuations induced by the vortex rope in the draft tube. The pressure fluctuations will not only cause variations in the power output, but also endangers other hydro turbine components, especially when its frequency approaches the natural frequency of the turbine [2]. Thus, knowledge of the dynamic load on the turbine is a major concern of the hydraulic community, and the simulation of flows in draft tubes has attracted attention during the past two decades. In order to accurately capture the flow features, efforts have been made by employing more advanced turbulence models, improving the grid quality and extending the computational domain to the complete hydro turbine. Guidelines to choose an appropriate turbulence model often begins from past numerical simulations and *a priori* knowledge of inherent flow features present in the flow. Presently, access to large computational resources have enabled the research community to employ increasingly resource-demanding models; from one-equation Reynolds-averaged Navier-Stokes (RANS) closure models to detached eddy simulation (DES) and large eddy simulation (LES). Early efforts to solve the RANS equations with the standard k-ε turbulence model [1, 3] were found to be over diffusive for the simulation of draft tube flows. Various alternative turbulence models for RANS have been applied, including the Reynolds Stress Model (RSM) [1,4,5,6] and the k-ω SST turbulence model [7,8,9]; however, there is no established consensus on which turbulence closure model is suitable to capture the complex flow field. Unlike RANS, in which all turbulence scales are modelled, LES resolves the large eddies and models the effect of small-scale turbulence through the use of subgrid-scale (SGS) models. Early LES attempts [10, 11, 12] employed coarse computational grids in the order of one to three million points that today would be classified as severely under resolved LES. Since the Reynolds number in the draft tube is on the level of 10^6, and the estimated grid-point requirement for wall-resolved LES is proportional to $Re_{L_x}^{13/7}$, then the computational domain should contain approximately 1.39×10^{11} grid points. As expected early results [10,11] did not improve upon prevailing RANS simulations but Guo et al. [12] captured the draft tube vortex rope frequency, resolved the axial and tangential velocity profiles downstream of the inlet, and acquired a reasonable agreement on the pressure pulsation against experimental data. The results may have been due to the use of accurate boundary conditions through the inclusion of the runner, then the accurate modelling of the turbulent flow field through the use of LES. This observation was further collaborated through an examination [6] of both a 23.5 million grid point LES and a 5.3 million grid point Unsteady RANS (URANS) simulation, where only the URANS simulation included a runner which, surprisingly yielded a more resolved vortex rope and frequency. Except neither produced an accurate measure of the pressure pulsation in the draft tube.

Since turbulence models are not the only determinant factor of numerical simulations, a thorough investigation should include the quality of the numerical grids and the role of numerical schemes. Initial grid studies [4, 9] demonstrated an enhanced amount of turbulent structures on finer grids and in [9] the turbulent kinetic energy spectra showed a well represented inertial range of turbulence at both the draft tube cone and diffuser. Magnan et al. [13] conducted the most extensive grid convergence study to date and assessed the impact on several global parameters and concluded that poor grid quality severely impacts the accuracy of turbulence models, where disparate averaged axial velocities and turbulent kinetic energy contours were observed.

Apart from turbulence models and grid effects, discretization schemes have a tremendous impact but their role has not been carefully examined in the context of draft tube flows. The proper resolution of fine turbulent structures not only require an appropriate time-step and grid spacing but a low dissipative scheme. This can be achieved through the use of high-order methods. Higher than second-order methods are currently intractable for draft tube flows due to the large Reynolds number and computational grid, but there is room for improvement in the development of novel low dissipative second-order schemes for vortex dominated or shear flow driven flows. Current second-order schemes employ reconstructions of the left and right states of the numerical fluxes to ensure the scheme remains second-order in smooth regions of the flow. However, variable reconstructions in second-order upwind schemes must be limited in regions of discontinuity or steep gradients to guarantee that no new maxima or minima are introduced. ANSYS FLUENT offers the Barth-Jespersen limiter, the Minmod limiter, and a modified Venkatakrishnan limiter, while ANSYS CFX employs the Barth-Jespersen limiter for its high resolution scheme. While the standard limiting prevents nonphysical oscillations near discontinuities, it also leads to a loss of accuracy near smooth extrema. To remedy this shortcoming, Venkatakrishnan [14] introduced a small non-vanishing differentiable parameter to prevent limiting near smooth extrema for the Barth-Jespersen limiter, while, Huynh [15] employed the ratio of two adjacent second-differences of density to discern smooth regions. Sekora and Colella [16] presented an approach that compared one-sided and centred estimates of the second-derivatives. If the estimates within a control volume are comparable, then the solution is smooth at the extremum; otherwise, it must be located near discontinuities, under-resolved gradients, or high-wavenumber oscillations [16].

In low-speed vortical flows, due to the presence of vortices, numerous smooth extrema exist in the fields of velocity components and static pressure. Similar to the extremum-preserving limiters, Löhner [17] developed a limiting algorithm to minimize the numerical dissipation of vorticity. Since the velocity typically reaches a local maximum in the tangential direction of the swirl plane, the slope limiter in second-order MUSCL schemes will switch the variable reconstruction from the first- to the zeroth-order, thereby resulting into an over-dissipation of the vortex. A helicity sen-

sor [17] is employed to identify vortical structures and the van Albada limiter in the swirl plane is inactivated to reduce the numerical dissipation. Mohamed, Nadarajah and Paraschvoiu [18] extended the approach and developed an eddy-preserving limiter for unsteady subsonic flows. The eddy-preserving limiter outperforms the minimal vorticity dissipation limiter [17] in three primary ways. First, in [17], the vortex axis is assumed to be perpendicular to the swirl plane, which lacks generality since turbulent structures undergo stretching and bending. Instead [18] employed the enhanced swirling strength criterion of Chakraborty et al. [19] for vortex-identification, which is based on the existence of complex eigenvalues for the velocity gradient tensor. Second, the principle direction of eddies are determined based on eigenvectors of the velocity gradient tensor, and no specific assumption regarding their relative orientation is made. Third, in addition to inactivating the slope limiter, the dissipation is further lowered via increasing the weight of central gradients during the velocity component reconstructions on the swirl plane of the vortex. With these features, the eddy-preserving limiter is more robust and capable of dealing with complex vortical flows. The development of DES and LES as well as access to large computing infrastructures have allowed researchers to demonstrate the efficacy of these numerical frameworks on large scale hydraulic turbine flows for the past several years [] Can you add a few recent citations here on hydraulic turbine flows. However, a reexamination of the impact of numerical dissipation in draft tube flows is warranted. In this paper, we extend the eddy-preserving limiter scheme by modifying the limiting algorithm for the interpolation of pressure, since a minimum pressure often exists along the axis of a free vortex. At smooth extrema of the pressure, the limiting is unnecessary and thus the conventional van Albada limiter is inactivated to reduce the dissipation. The smooth region of pressure is detected by comparing the neighbouring second difference of pressure, a criterion proposed by Huynh [15]. The effects of the original and extended eddy-preserving limiter scheme are initially demonstrated for a three-dimensional inviscid vortex advection and the three-dimensional convection of a vortex whose axis is parallel to the flow. We then apply the developed scheme for the simulation of the BulbT [20] test case.

2 Methodology

2.1 Governing Equations

Consider the three-dimensional compressible Navier-Stokes equations using Einstein notation,

$$\frac{\partial \mathbf{W}}{\partial t} + \frac{\partial \mathbf{F}_i}{\partial x_i} - \frac{\partial \mathbf{F}_{\mathbf{v}i}}{\partial x_i} = 0, \tag{1}$$

where the state vector $\mathbf{W}$, the inviscid fluxes $\mathbf{F}_i$, and the viscous fluxes $\mathbf{F}_{\mathbf{v}i}$ are given by,

$$\mathbf{W} = \begin{pmatrix} \rho \\ \rho u_1 \\ \rho u_2 \\ \rho u_3 \\ \rho E \end{pmatrix}, \mathbf{F}_i = \begin{pmatrix} \rho u_i \\ \rho u_1 u_i + p\delta_{i1} \\ \rho u_2 u_i + p\delta_{i2} \\ \rho u_3 u_i + p\delta_{i3} \\ \rho E u_i + p u_i \end{pmatrix}, \mathbf{F}_{\mathbf{v}i} = \begin{pmatrix} 0 \\ \tau_{ij}\delta_{i1} \\ \tau_{ij}\delta_{i2} \\ \tau_{ij}\delta_{i3} \\ u_j\tau_{ij} + \kappa\frac{\partial T}{\partial x_i} \end{pmatrix}. \tag{2}$$

In the above equations, ρ, p and T are the density, pressure, and temperature respectively. The specific total energy is denoted by E and $\mathbf{u} = [u_1, u_2, u_3]^T$ is the velocity vector. τ_{ij} is the viscous stress and δ_{ij} is the Kronecker delta function. The governing equations are solved with an in-house second-order finite-volume approach and the k-ω SST turbulence model. Three schemes, i. e. MUSCL, original eddy-preserving limiter, and extended eddy-preserving limiter schemes, are employed for the spatial discretization, and will be described in later subsections. For unsteady simulations, dual time stepping and a second-order backward difference formula (BDF) are employed. The solution is advanced with Jameson's five-stage modified Runge-Kutta method. Local time-stepping and multigrid techniques, as well as implicit residual smoothing, are utilized to speed up the convergence.

2.2 Equation of State

To simulate incompressible hydro-turbine flows, the stiffened gas law is employed as the equation of state, which is given by,

$$p = (\gamma - 1)\rho e - \gamma p_\infty, \tag{3}$$

and the speed of sound is computed by,

$$c = \sqrt{\gamma \frac{p + p_\infty}{\rho}}. \tag{4}$$

The specific heat ratio, γ and p_∞ are two parameters used to define liquids with different properties. The stiffened gas equation of state can provide a reasonable approximation for liquids under high pressure conditions. For water, values for γ and p_∞ used by various authors are listed in Table 1. In this paper, to respect the physical speed of sound in water at $20\,^\circ$C, γ and p_∞ are chosen to be 7.15 and 3.1×10^8 Pa respectively.

2.3 Low-Speed Preconditioning

As a consequence of the large speed of sound, the Mach number is typically very low which makes the system difficult to converge. To alleviate this problem, a low-speed preconditioner [30] is implemented in this work.

$$\mathbf{P}^{-1}\frac{\partial \mathbf{W}}{\partial t} + \mathbf{R}(\mathbf{W}) = 0. \tag{5}$$

Table 1. Parameters for stiffened gas law used by various authors.

Authors	γ	p_∞ ($\times 10^8$ Pa)	c (m/s)
Goncalves & Patella [21]	1.01	0.1211	110.7
Chang & Liou [22]	1.932	11.645	1482
Le Métayer et al. [23]	2.35	10.0	1533
Paillere et al. [24]	2.8	8.5	1543
Barberon & Helluy [25]	3.0	8.533	1600
Saurel & Abgrall [26]	4.4	6.0	1626
Shyue [27]	7.0	3.0	1449
Luo et al. [28]	7.0	3.03975	1459
Gallouët et al. [29]	7.15	3.0	1465
Present paper	7.15	3.1	1489

The preconditioner for the entropy variables $\mathbf{W}_0 = [p, u, v, w, S]^T$ is

$$\mathbf{P}_0 = \begin{pmatrix} \beta^2 & 0 & 0 & 0 & 0 \\ 0 & 1 & 0 & 0 & 0 \\ 0 & 0 & 1 & 0 & 0 \\ 0 & 0 & 0 & 1 & 0 \\ 0 & 0 & 0 & 0 & 1 \end{pmatrix}. \qquad (6)$$

Since the conservative variables are used in the present work, the preconditioner $\mathbf{P}$ for the conservative variables $\mathbf{W} = [\rho, \rho u, \rho v, \rho w, \rho E]^T$ can be computed by,

$$\mathbf{P} = \frac{\partial \mathbf{W}}{\partial \mathbf{W}_0} \mathbf{P}_0 \frac{\partial \mathbf{W}_0}{\partial \mathbf{W}}. \qquad (7)$$

For optimal preconditioning, β^2 should be proportional to the square of the local Mach number M, a reference Mach number M_{ref} is used to avoid singularities at stagnation points. Then the value of β^2 is modified to account for the viscous effects,

$$\beta^2_{inv} = K_1 M^2 + K_2 M^2_{ref}, \qquad (8)$$
$$\beta^2_{vis} = (1 + 2Re_{\Delta x}^{1/3})\beta^2_{inv}, \qquad (9)$$

where $Re_{\Delta x}$ is the cell Reynolds number, K_1 and K_2 are constants and set to be 1.0 in this paper. The final value for β^2 must be less or equal to unity,

$$\beta^2 = \min(\beta^2_{vis}, 1.0). \qquad (10)$$

When β^2 equals unity, $\mathbf{P}$ is an identity matrix and the preconditioner is switched off.

2.4 Monotonic Upstream-centered Scheme for Conservation Laws (MUSCL)

In the MUSCL scheme, the primitive variables $\mathbf{V} = [\rho, u_1, u_2, u_3, p]^T$ are interpolated at the interfaces of cell i and cell $i+1$ using,

$$\mathbf{V}^L_{i+\frac{1}{2}} = \mathbf{V}_i + \frac{\Phi_i}{4}[(1-\kappa)\Delta^u_{i-\frac{1}{2}}\mathbf{V} + (1+\kappa)\Delta^c_{i+\frac{1}{2}}\mathbf{V}], \qquad (11)$$

$$\mathbf{V}^R_{i+\frac{1}{2}} = \mathbf{V}_{i+1} - \frac{\Phi_{i+1}}{4}[(1-\kappa)\Delta^u_{i+\frac{3}{2}}\mathbf{V} + (1+\kappa)\Delta^c_{i+\frac{1}{2}}\mathbf{V}], \qquad (12)$$

where Φ_i and Φ_{i+1} are slope limiters, and $-1 \le \kappa \le 1$. The upwind and central increments are computed by,

$$\Delta^u_{i-\frac{1}{2}}\mathbf{V} = \mathbf{V}_i - \mathbf{V}_{i-1} \quad \text{and} \quad \Delta^u_{i+\frac{3}{2}}\mathbf{V} = \mathbf{V}_{i+2} - \mathbf{V}_{i+1}, \qquad (13)$$

$$\Delta^c_{i+\frac{1}{2}}\mathbf{V} = \mathbf{V}_{i+1} - \mathbf{V}_i, \qquad (14)$$

where the superscripts u and c denotes either upwind or central increments. In our baseline MUSCL scheme, $\kappa = \frac{1}{3}$ and the van Albada limiter is employed,

$$\Phi(R) = \begin{cases} \frac{2R}{R^2+1}, & \text{if } R > 0 \\ 0, & \text{if } R \le 0 \end{cases}, \text{ where } R_i = \frac{\mathbf{V}_{i+1} - \mathbf{V}_i}{\mathbf{V}_i - \mathbf{V}_{i-1}}. \qquad (15)$$

When κ is further increased, the artificial dissipation decreases. In the limit, where $\kappa = 1$, a purely central but unstable convective flux calculation scheme is obtained.

2.5 Eddy-Preserving Limiter Scheme

The concept of the eddy-preserving limiter is to prevent the slope limiter to be activated (or to use a less dissipative limiter) during the reconstruction of the velocity component along the tangential direction of a vortex. To identify vortical flow regions, the enhanced swirling strength criterion of Chakraborty et al. [19] is employed, whereby in a vortical region, the velocity gradient tensor $\nabla \mathbf{v}$ possesses a conjugate pair of complex eigenvalues,

$$\sigma(\nabla \mathbf{v}) = \{\lambda_r, \lambda_{cr} + i\lambda_{ci}, \lambda_{cr} - i\lambda_{ci}\}, |\lambda_{ci}| > \varepsilon, \qquad (16)$$

where ε is a small positive real number. A local measure for the compactness of the vortical motion is added to further limit the vortical regions to areas where the following condition is satisfied,

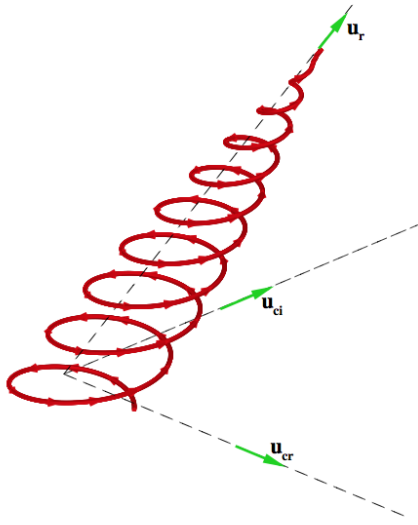$$-\zeta \le \frac{\lambda_{cr}}{\lambda_{ci}} \le \delta, \qquad (17)$$

Fig. 1. Illustration of the vortex system [18].

where ζ and δ are positive thresholds for verifying the compactness of the vortex. The velocity gradient tensor can be decomposed into the following form,

$$\nabla \mathbf{v} = \begin{bmatrix} \hat{\mathbf{u}}_r \ \hat{\mathbf{u}}_{cr} \ \hat{\mathbf{u}}_{ci} \end{bmatrix} \begin{bmatrix} \lambda_r & 0 & 0 \\ 0 & \lambda_{cr} & \lambda_{ci}\frac{|\mathbf{u}_{cr}|}{|\mathbf{u}_{ci}|} \\ 0 & -\lambda_{ci}\frac{|\mathbf{u}_{ci}|}{|\mathbf{u}_{cr}|} & \lambda_{cr} \end{bmatrix} \begin{bmatrix} \hat{\mathbf{u}}_r \ \hat{\mathbf{u}}_{cr} \ \hat{\mathbf{u}}_{ci} \end{bmatrix}^{-1},$$
(18)

where $\hat{\mathbf{u}}_r$, $\hat{\mathbf{u}}_{cr}$, and $\hat{\mathbf{u}}_{ci}$ are normalized eigenvectors of the velocity gradient tensor. The mapping and transformation matrix from the original Cartesian system $\mathbf{S}_0$ to the local vortex system $\mathbf{S}_\omega$ spanned by $\hat{\mathbf{u}}_r$, $\hat{\mathbf{u}}_{cr}$, and $\hat{\mathbf{u}}_{ci}$, are given by,

$$\begin{bmatrix} \hat{\mathbf{M}} \end{bmatrix} : \mathbf{S}_0 \mapsto \mathbf{S}_\omega \quad \begin{bmatrix} \hat{\mathbf{M}} \end{bmatrix} = \begin{bmatrix} \hat{\mathbf{u}}_r \ \hat{\mathbf{u}}_{cr} \ \hat{\mathbf{u}}_{ci} \end{bmatrix}^{-1}.$$
(19)

The algorithm for the eddy-preserving limiting procedure is described below:

1. Calculate eigenvalues of the velocity gradient tensor $\nabla \mathbf{v}$. If the velocity gradient tensor has only real eigenvalues, then exit and employ the conventional van Albada limiter.
2. Verify the compactness of the vortical motion using Eqn. 17. If the flow lacks vortical compactness, then exit and employ the conventional van Albada limiter.
3. Calculate eigenvectors of the velocity gradient tensor $\nabla \mathbf{v}$, and define the transformation matrix $\begin{bmatrix} \hat{\mathbf{M}} \end{bmatrix}$.
4. Transform velocity components into the vortex system $\mathbf{S}_\omega$.
5. In the axial direction, reconstruct variables using the conventional van Albada limiter with $\kappa = \frac{1}{3}$.
6. In the swirl plane, reconstruct variables using a higher κ which leads to less artificial dissipation and inactivate the van Albada limiter by setting $\Phi_i = \Phi_{i+1} = 1$.

7. Transform interpolated velocity components back to the original system $\mathbf{S}_0$ and evaluate the fluxes.

2.6 Extended Eddy-Preserving Limiter Scheme

To extend the eddy-preserving limiter, the van Albada limiter for the interpolation of pressure is switched off at smooth extrema. By setting $\Phi_i = \Phi_{i+1} = 1$, the interpolation for pressure at smooth extrema is given by,

$$p_{i+\frac{1}{2}}^L = p_i + \frac{1}{4}[(1-\kappa)\Delta_{i-\frac{1}{2}}^u p + (1+\kappa)\Delta_{i+\frac{1}{2}}^c p],$$
(20)

$$p_{i+\frac{1}{2}}^R = p_{i+1} - \frac{1}{4}[(1-\kappa)\Delta_{i+\frac{3}{2}}^u p + (1+\kappa)\Delta_{i+\frac{1}{2}}^c p].$$
(21)

The smooth extrema is detected based on a criterion proposed by Huynh [15]. If the solution is smooth at the extremum, then the second-difference in neighbouring cells are comparable. Define the second-difference of p as,

$$\Delta_i^2 p = p_{i-1} - 2p_i + p_{i+1}.$$
(22)

If the following conditions are satisfied,

$$\frac{4}{5} \le \frac{\Delta_{i-1}^2 p}{\Delta_i^2 p} \le \frac{5}{4},$$
(23)

$$\frac{4}{5} \le \frac{\Delta_{i+1}^2 p}{\Delta_i^2 p} \le \frac{5}{4},$$
(24)

then the extremum is considered to be smooth, and the limiting is unnecessary. As remarked by Huynh [15], the factors $\frac{4}{5}$ and $\frac{5}{4}$ can be relaxed to $\frac{2}{3}$ and $\frac{3}{2}$ for the case of linear convection.

3 Numerical Results
3.1 Three Dimensional Inviscid Vortex Advection

An inviscid vortex advection case is designed to demonstrate the effects of the eddy-preserving limiter schemes. The direction of advection is perpendicular to the vortex surface, as illustrated in Fig. 2. The flow field is initialized as an isentropic vortex superimposed by a uniform flow, where $u_\infty = 0$, $v_\infty = 0$ and $w_\infty = 1$. The flow variables are computed by:

$$\rho = [1 - \frac{(\gamma-1)\beta^2}{8\gamma\pi^2}e^{1-r^2}]^{1/(\gamma-1)},$$

$$u = u_\infty + \delta u = -\frac{\beta y}{2\pi}e^{(1-r^2)/2},$$

$$v = v_\infty + \delta v = \frac{\beta x}{2\pi}e^{(1-r^2)/2},$$

$$w = w_\infty,$$

$$p = \rho^\gamma,$$
(25)

where the centre of the vortex is located at $(x, y) = (0, 0)$, $r = \sqrt{x^2 + y^2}$ represents the distance to the centre of the vortex, and β is the vortex strength and is set to a value of 5.
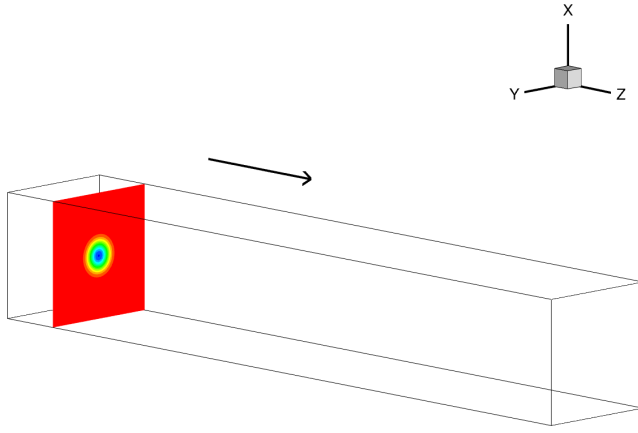
Fig. 2. Illustration of the vortex advection.

The geometry of the computational domain is a rectangular box, where $-5 \leq x \leq 5$, $-5 \leq y \leq 5$, and $0 \leq z \leq 12$. We demonstrate the ability of the schemes to preserve the vortex through a grid refinement study, where the coarse grid has dimensions $\Delta x = \Delta y = \Delta z = 0.5$, the medium grid with $\Delta x = \Delta y = \Delta z = 0.25$, and the fine grid with $\Delta x = \Delta y = \Delta z = 0.125$. The time step is set to be $\Delta t = 0.04$ and the final time is $t = 10$. The test cases are simulated with the baseline MUSCL scheme, the original and the extended eddy-preserving limiter schemes. The computed results are denoted by "MUSCL", "EDDY", and "EDDY-P" respectively.

The profiles of the x component of velocity at $x = 0$ and several time instances $t = 2$, $t = 6$, and $t = 10$ are shown in Fig. 3. The relative L^2 norms of the error are plotted in Fig. 5 (a). The profiles computed by the EDDY and EDDY-P schemes are similar, and hence the modification for the interpolation of pressure has little impact on the velocity profiles. The predictions of both the EDDY and EDDY-P schemes agree better against the exact solutions when compared to the MUSCL scheme, due to their lower numerical dissipations.

The pressure profiles at $x = 0$ and several time instances $t = 2$, $t = 6$, and $t = 10$ are shown in Fig. 4, while the relative L^2 norms of the error are plotted in Fig. 5 (b). The EDDY scheme outperforms the MUSCL scheme, while the EDDY-P scheme demonstrates a slight further improvement, which shows that the modification for the interpolation of pressure is able to further reduce the dissipation.

The vortex core regions on the medium grid for all schemes are represented by the contour lines of $Q = 0$, as shown in Fig. 6. As time advances, the vortex core of the MUSCL scheme grows, while that of the EDDY and EDDY-P are maintained, which demonstrates the schemes ability to preserve the vortex due to their lower dissipation.

A study of accuracy was performed for all three schemes on four consecutively refined grids. The L^2 error of pressure at $t = 2$ with respect to the grid spacing is plotted in Fig. 7. The slopes of all three schemes are able to match the slope of the referenced 2nd-order line as the grid is refined.

3.2 Three Dimensional Viscous Vortex Advection

A viscous vortex advection case is performed on a grid, where $\Delta x = \Delta y = \Delta z = 0.25$ and $-5 \leq x \leq 5$, $-5 \leq y \leq 5$, and $0 \leq z \leq 24$. A vortex profile is fixed at the inlet, where the density and velocity profiles are prescribed according to Eqn. 25, and the pressure is set to be constant at the outlet. Periodic boundary conditions are imposed for the remaining boundaries. The Reynolds number is set to 1.56×10^6. The vortex is expected to be dissipated in the stream-wise more severely than the inviscid cases, and the isosurface of vorticity magnitude would resemble a cone.

The test cases are simulated with the baseline MUSCL scheme, the original and the extended eddy-preserving limiter schemes. The unsteady simulations for all schemes start from a converged steady solution computed from the MUSCL scheme. The time step is set to be constant $\Delta t = 0.04$, and at final time $t = 20$, all simulations have reached quasi-steady states.

The vorticity contours at several stream-wise locations are plotted in Fig. 8. At each location, the EDDY and EDDY-P schemes produce higher vorticity magnitude in the central region than the MUSCL scheme. The isosurface of vorticity with magnitude unity is plotted in Fig. 9 to illustrate the vortex. The EDDY and EDDY-P schemes are able to preserve the vortex considerably longer than the MUSCL scheme. The comparisons demonstrate that the EDDY and EDDY-P schemes also outperform the MUSCL scheme for the benchmark turbulent flow simulation.

3.3 BulbT Test Case
3.3.1 Case Description

The BulbT project was initiated at the "Laboratoire de Machines Hydrauliques" (LAMH) of Laval University, and aimed at investigating the flow phenomena in a bulb turbine [20]. The turbine model consists of an intake, a bulb and a draft tube, as illustrated in Fig. 10. The experiments were conducted at five Operating Points (OP) as shown in Fig. 11; where OP2 is closest to the best efficiency point (BEP), and the flow phenomenon is less complex compared to other OPs. Therefore, in this work, OP2 is chosen for validating the proposed schemes.

The geometry of the draft tube is shown in Fig. 12. The draft tube is composed of two parts, a conical and a transition part. The conical part has a divergence angle of $10.25°$ and a length of 1.4 times the diameter of the runner shroud, D_{ref}. The transition part transforms the cross section from a circular shape to a rectangular shape. It has a length of $2.3D_{ref}$ and it is not symmetric. The divergence angles are $9.5°$ on the left and right sides, and $5°$ on the bottom side, while the top side is near horizontal.

The numerical simulations were performed on three consecutively refined grids, which consist of 3M, 14M and 50M cells respectively. The grid only consists of the hub, the draft tube and an extension as shown in Fig. 13. The extension is added to ensure that the flow discharges to the reservoir at ambient conditions. A sideview, and the inlet and outlet of the 14M grid are shown in Fig. 14. In Fig. 15, the
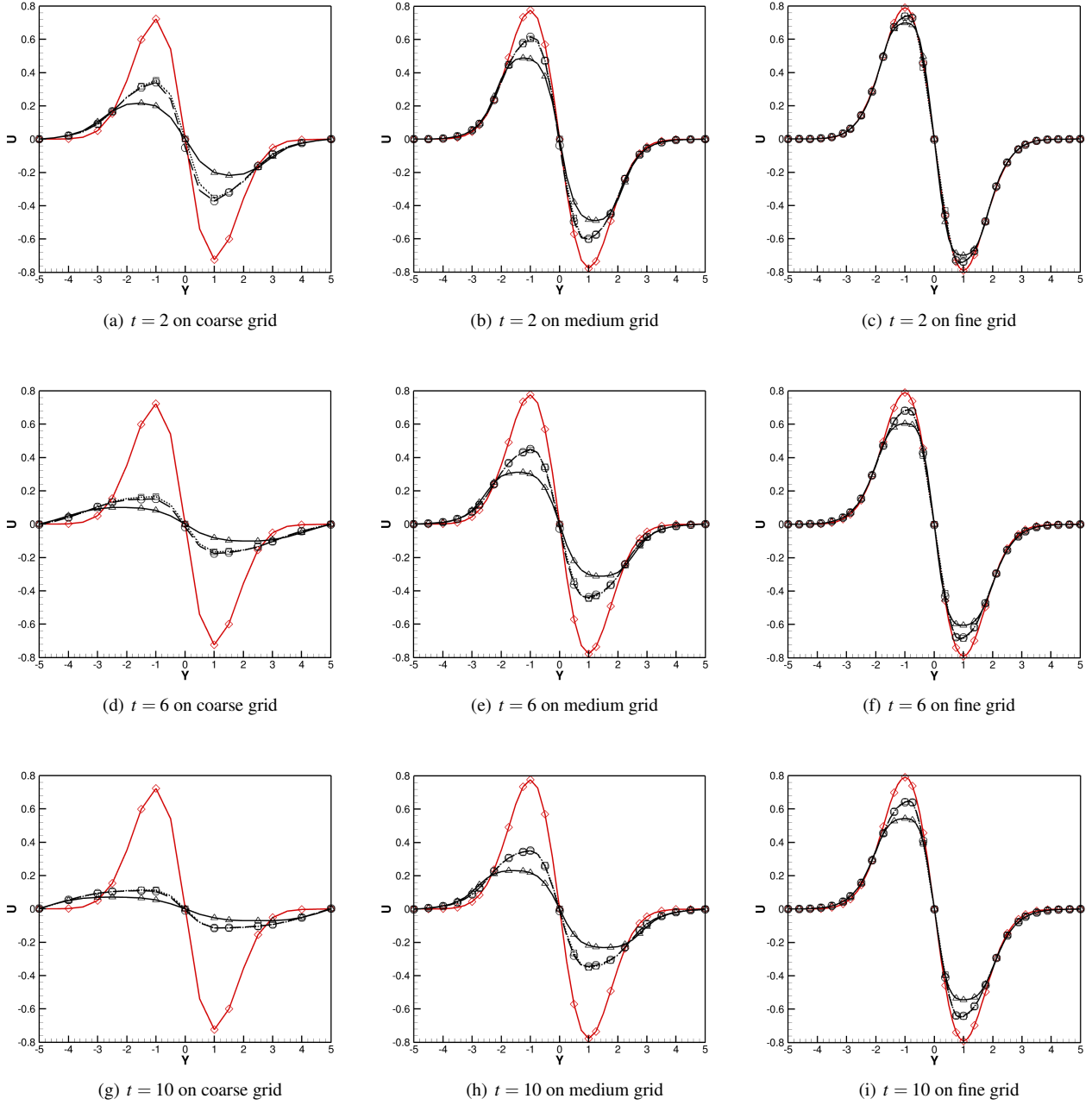
(a) $t = 2$ on coarse grid   (b) $t = 2$ on medium grid   (c) $t = 2$ on fine grid

(d) $t = 6$ on coarse grid   (e) $t = 6$ on medium grid   (f) $t = 6$ on fine grid

(g) $t = 10$ on coarse grid   (h) $t = 10$ on medium grid   (i) $t = 10$ on fine grid

Fig. 3.   Velocity profiles at $x = 0$. (MUSCL: ——△——; EDDY: ··▫··; EDDY-P: –⊖– ; Exact: —◇—.)

zoom-in view illustrates that central regions downstream of the hub and near-wall regions are refined, in order to better capture the flow features. The first cells close to the wall are placed at $y^+ \approx 1$ for all three grids.

No-slip boundary conditions are applied to all solid walls on the rotating hub and the stationary draft tube, while slip boundary conditions are imposed on the solid walls of the extension. The inlet profile is extracted from a numerical simulation conducted with the complete turbine. At the outlet, a zero pressure boundary condition is imposed. The numerical simulations were performed with the baseline MUSCL scheme, the original and extended eddy-preserving limiter scheme. The dissipation of all three schemes were scaled down with a factor of $\alpha = 0.375$ in computing the convective flux,

$$\mathbf{F}_{i+\frac{1}{2}} = \frac{1}{2}(\mathbf{F}(\mathbf{W}^L_{i+\frac{1}{2}}) + \mathbf{F}(\mathbf{W}^R_{i+\frac{1}{2}}) - \alpha \mathbf{P}^{-1}\lambda(\mathbf{W}^R_{i+\frac{1}{2}} - \mathbf{W}^L_{i+\frac{1}{2}})),$$

(26)

where λ is the spectral radius of the preconditioned Jacobian. The numerical results computed by the three schemes are denoted by "MUSCL", "EDDY", and "EDDY-P" respectively.

(a) $t = 2$ on coarse grid

(b) $t = 2$ on medium grid

(c) $t = 2$ on fine grid

(d) $t = 6$ on coarse grid

(e) $t = 6$ on medium grid

(f) $t = 6$ on fine grid

(g) $t = 10$ on coarse grid

(h) $t = 10$ on medium grid

(i) $t = 10$ on fine grid
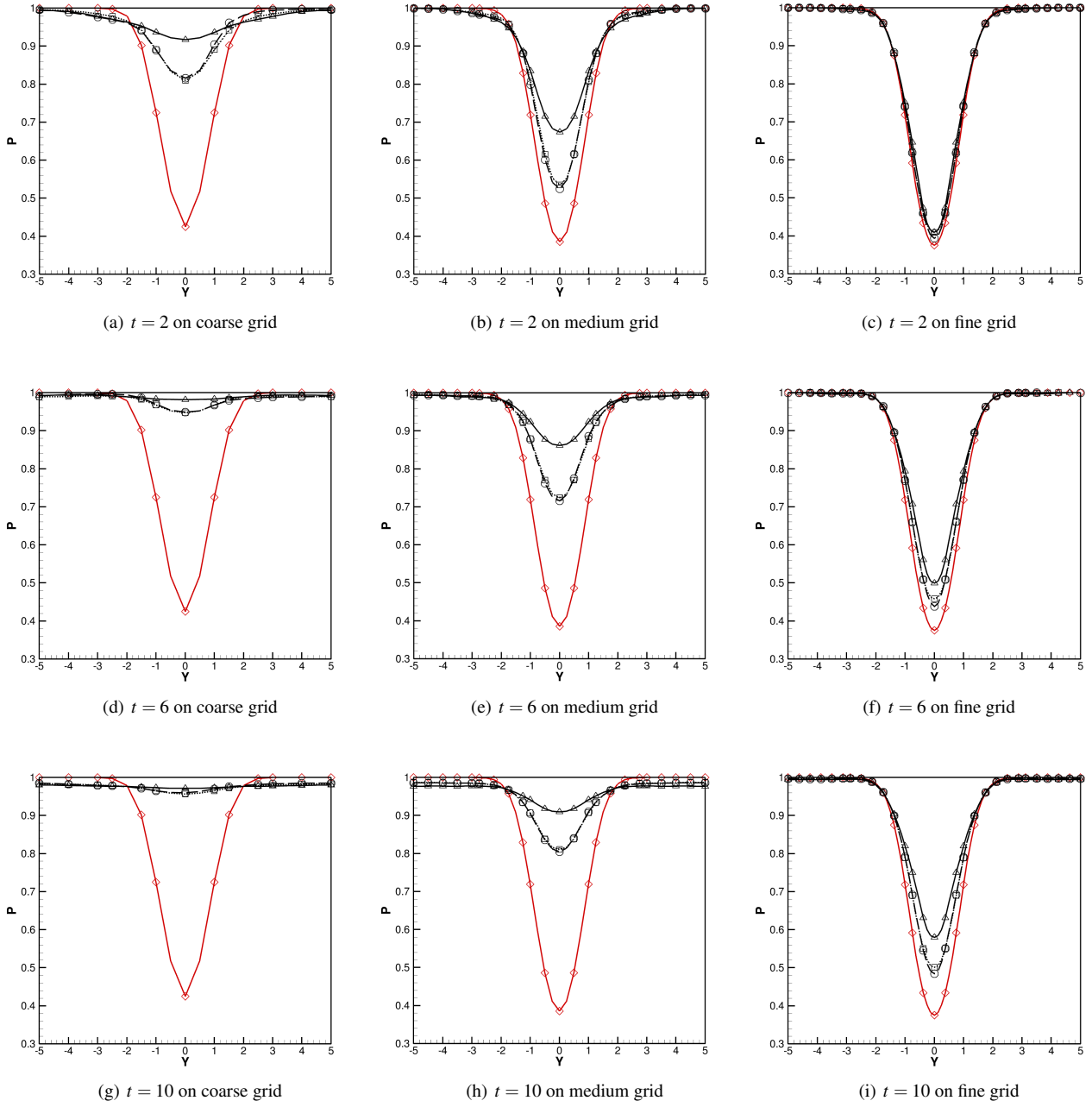
Fig. 4. Pressure profiles at $x = 0$. (MUSCL: —△—; EDDY: ··☐··; EDDY-P: -⊖- ; Exact: —◇—.)

3.3.2 Velocity Profiles

In the experiment, the axial and circumferential velocity profiles were measured by the Laser Doppler Velocimetry (LDV) along $y = 0$ of Plane 4B, which is the green line labeled as Axis B in Fig. 16. This location is referred as 4BY0.

As shown in Fig. 17 and Fig. 19, the global trends of the experimental axial and circumferential velocities are captured, and on each grid, the velocity profiles computed by all schemes are almost identical. However, zoom-in views of the velocity profiles show some discrepancies in the central region.

In the zoom-in view of the axial velocity profile in Fig. 18, the experimental data shows a backflow downstream

of the hub [31]. The MUSCL scheme shows poor predictions of the backflow region on all three grids. Although EDDY and EDDY-P schemes predict similar profiles to the MUSCL scheme on the 3M grid, they are able to resolve the backflow region on the 14M and 50M grids, and the predictions improve towards the experimental data as the grid was refined. Furthermore, the backflow predicted by the EDDY-P scheme is slightly closer to the experimental data than the EDDY scheme.

As for the experimental circumferential velocity, three zones are clearly identified: an inner co-rotating zone downstream of the hub; an outer co-rotating zone from the cone wall; and a counter-rotating zone in-between [31]. The cir-
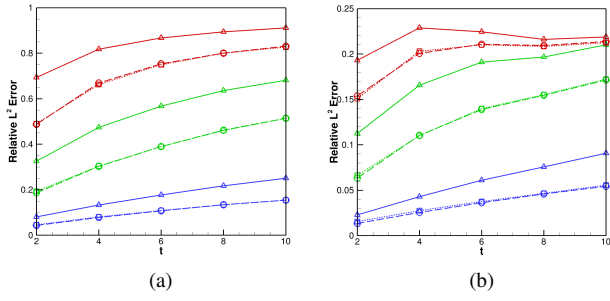
Fig. 5. Relative L^2 error of (a)velocity (b)pressure. (Coarse grid: MUSCL: —△—; EDDY: ··□··; EDDY-P: –⊖– . Medium grid: MUSCL: —△—; EDDY: ··□··; EDDY-P: –⊖– . Fine grid: MUSCL: —△—; EDDY: ··□··; EDDY-P: –⊖– .)
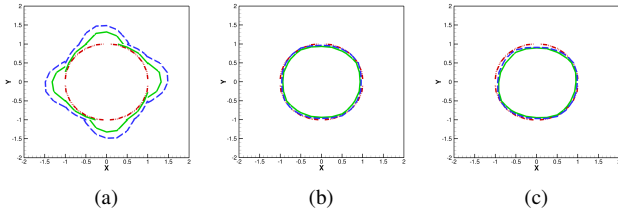
Fig. 6. $Q = 0$ contour lines on medium grid for (a)MUSCL (b)EDDY (c)EDDY-P schemes. ($t = 0$: –·–·; $t = 4$: ——; $t = 8$: – – –.)
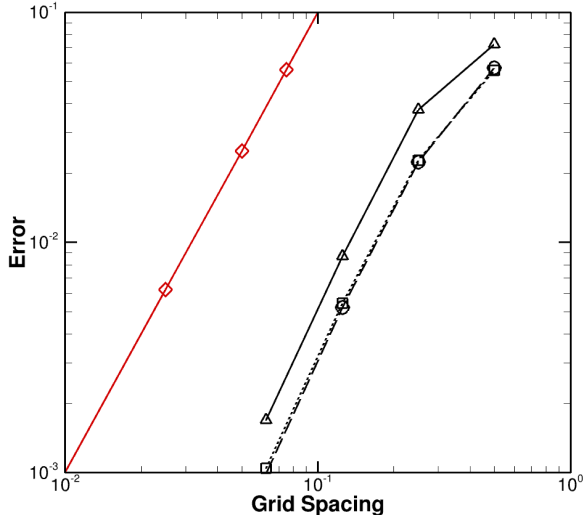
Fig. 7. Accuracy study of different schemes. (MUSCL: —△—; EDDY: ··□··; EDDY-P: –⊖– ; 2nd-order: –◇–.)

(a) MUSCL at $z = 1$ (b) EDDY at $z = 1$ (c) EDDY-P at $z = 1$

(d) MUSCL at $z = 2$ (e) EDDY at $z = 2$ (f) EDDY-P at $z = 2$

(g) MUSCL at $z = 3$ (h) EDDY at $z = 3$ (i) EDDY-P at $z = 3$

Fig. 8. Vorticity contours at different locations for three schemes.

cumferential velocity first accelerates from the centre point in the direction of the runner rotation gently to a local maximum, which represents a forced vortex induced by the rotating hub. It then decelerates to zero, where the flow rotational direction is reversed, and the inner co-rotating zone is formed from the centre point to this position. The circumferential velocity then subsequently accelerates in the reversed direction to a local maximum and then decelerates. It continues to decelerate to zero and forms the counter-rotating zone. A shear flow is formed by the inner co-rotating zone and the counter-rotating zone at approximately $x = \pm0.023$. The flow then changes to a co-rotating direction until it reaches the cone wall. The zoom-in view in Fig. 20 shows the circumferential velocity in the inner co-rotating zone and the counter-rotating zone. All schemes do not predict the circumferential velocity very well in the central region on the 3M grid. On the 14M and 50M grids, although the MUSCL scheme has improved slightly, it still behaves poorly from the centre point to the position of maximum velocity in the counter-rotating zone; in comparison, the EDDY and EDDY-P schemes predict better the locations and the magnitudes of the maximum velocities.

Figure 21 and Figure 22 show the contours of axial velocity and two dimensional streamlines at plane $y = 0$ on 14M and 50M grids. The axial velocity decelerates rapidly from the inlet to the end of the hub, as the cross section expands drastically. Flow separation takes place on the wall of the hub and a backflow region is formed downstream of the hub. Comparing the results of the MUSCL scheme against the EDDY and EDDY-P schemes, it can be clearly seen that the EDDY and EDDY-P schemes predict a wider and longer backflow region fully attached to the hub. After the hub, the flows merge into one and continue to decelerate, but at a slower rate.

There are several challenges for numerical schemes in predicting the velocity profiles at 4BY0. For the axial velocity, it has a local minimum and a backflow region, while for the circumferential velocity, there are two co-rotating and
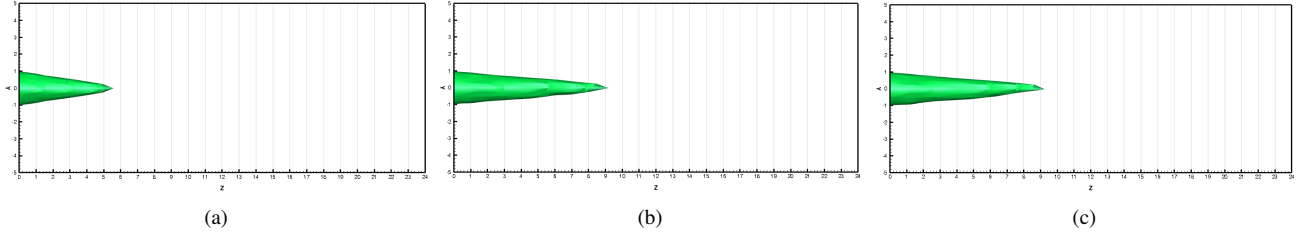
Fig. 9.   Isosurface of vorticity magnitude computed by three schemes at $t = 20$. (a)MUSCL (b)EDDY (c)EDDY-P.
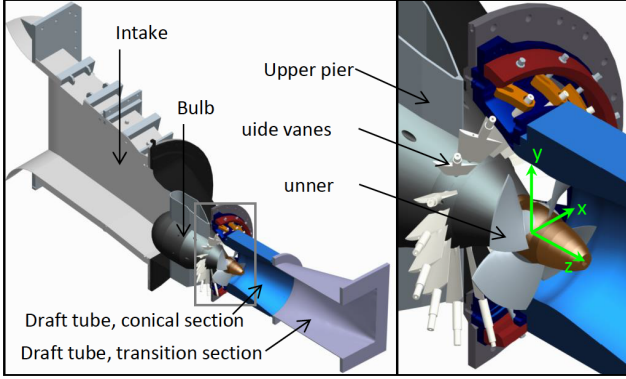
Fig. 10.   Turbine model of BulbT [31].

Fig. 12.   Geometry of the draft tube [32].

Fig. 11.   Operating points of BulbT [31].
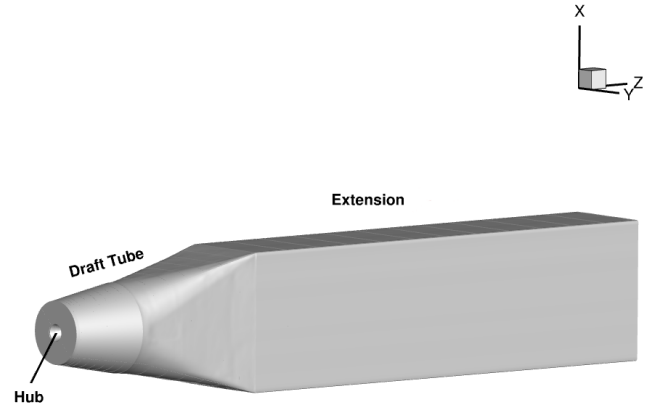
Fig. 13.   Geometry of the grid.

one counter-rotating zone. The velocity components are constrained by the divergence free condition for incompressible flows. Furthermore, the adverse pressure gradient needs to be accurately resolved to ensure that the flow decelerates appropriately, and the flow separation takes place at the correct location. Tackling these challenges requires highly accurate numerical schemes, and the comparisons illustrate that the MUSCL scheme generally fails to predicting these features, while the developed low dissipative EDDY and EDDY-P schemes have outperformed significantly over the MUSCL scheme.

3.3.3   Turbulent Kinetic Energy Profiles

The results for the turbulent kinetic energy (TKE) at 4BY0 are plotted in Fig. 23. There are several peaks found in the experimental profile. Two higher peaks at approxi-

mately $x = \pm 0.023$ corresponds to the shear flows formed by the inner co-rotating zone and the counter-rotating zone. Two lower peaks corresponds to the shear layer near the cone walls. Overall, the TKE profiles were underpredicted by all schemes in most of the region. In the zoom-in view of Fig. 24, incorrect TKE peaks appear in the central region, which are mainly due to the large gradients of the computed velocity profiles in Fig. 20. As the grid was refined, the predictions of flows downstream of the hub have improved, leading to a reduction of the incorrect TKE peak at the central core; while the shear flow has been better formed between the inner co-rotating zone and the counter-rotating zone, the two side peaks edge upwards, showing a clear improvment towards the experimental data. On each grid, compared to the MUSCL scheme, the EDDY and EDDY-P schemes predict slightly higher values at the two side peaks
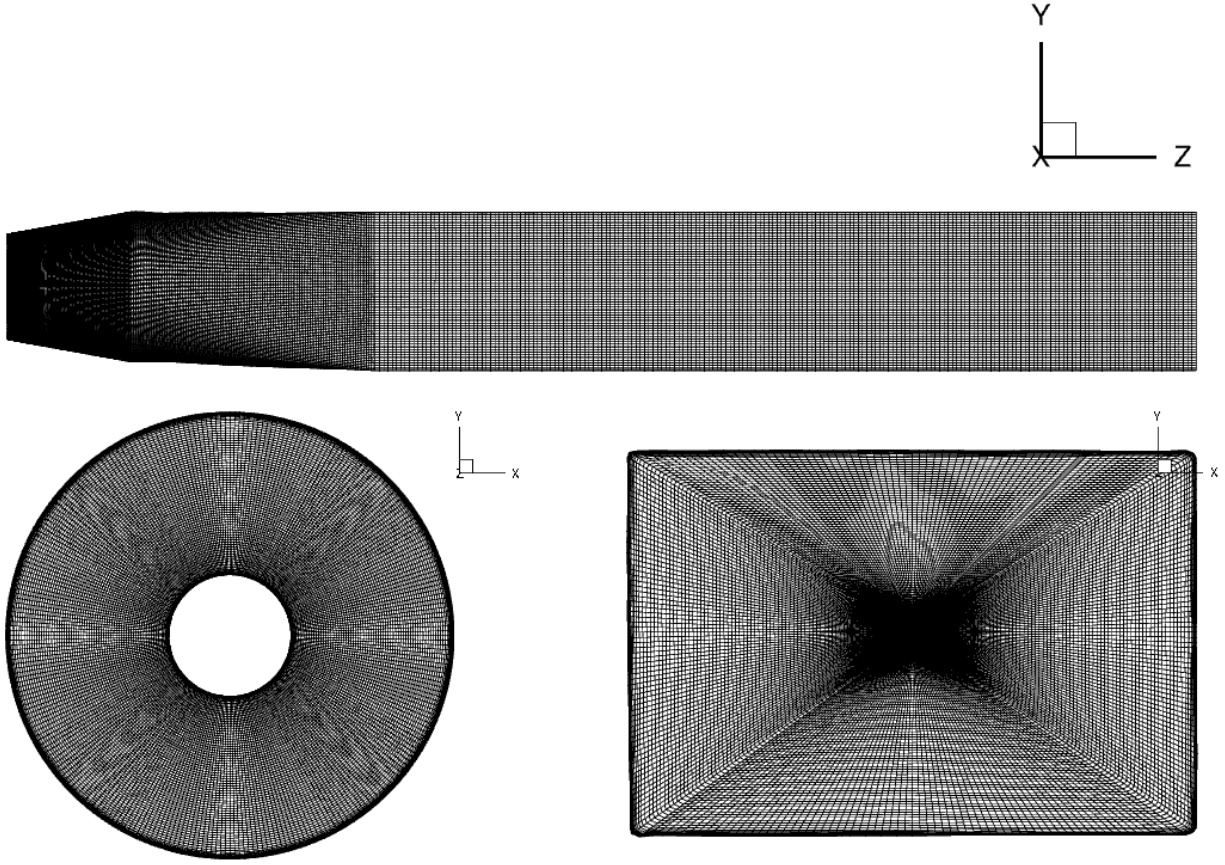
Fig. 14.   Overview of the 14M grid.

(a)

(b)

(c)
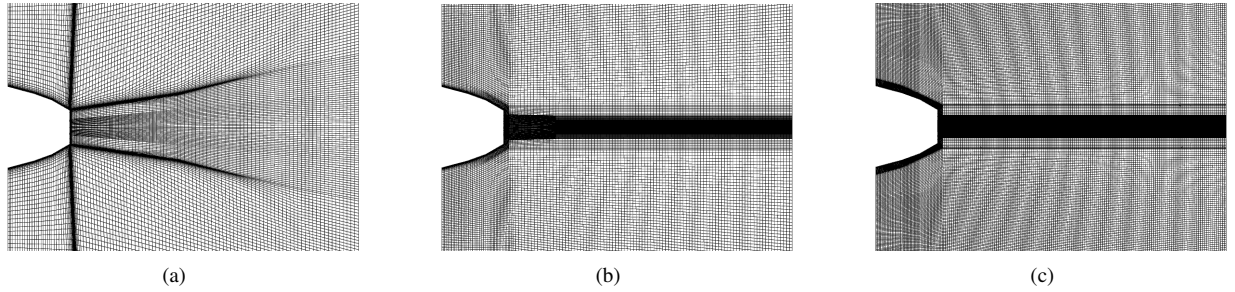
Fig. 15.   Zoom-in view of the (a)3M (b)14M (c)50M grid.

and lower values in the central core region, which leads to better agreement against the experimental data.

3.3.4   Vorticity Magnitude Profiles

The profiles of the vorticity magnitude in the central region of 4BY0 are plotted in Fig. 25. Due to lack of an experimental radial velocity profile, the experimental vorticity magnitude was computed with the assumption that the flow is uniform in the circumferential direction. This is certainly not what would be observed in the experimental data; however, this assumption is sufficient for the purpose of comparing numerical schemes.

Three peaks are shown in the experimental profile. The central peak represents the forced vortex induced by the rotating hub, while the two side peaks at approximately $x = \pm 0.023$ represent the shear flows formed by the inner co-rotating zone and the counter-rotating zone. Since OP2 is close to the BEP, the draft tube flow is expected to have very weak swirls. This can be seen from the experimental data in Fig. 20, where the circumferential profiles near the centre point have very gentle slopes. On the 3M grid, all schemes overpredict the vorticity magnitude in the centre, due to the mispredicted gradients of the circumferential velocity, as shown in Fig. 20(a). The overprediction of the vorticity in the central region partially contributes to the overproduction of the TKE in Fig. 24, which will result in excessive dissipation, and deteriorate the predictions of velocity profiles downstream of the hub. On the 14M and 50M grids, the MUSCL scheme still overpredicts the peak in the centre,
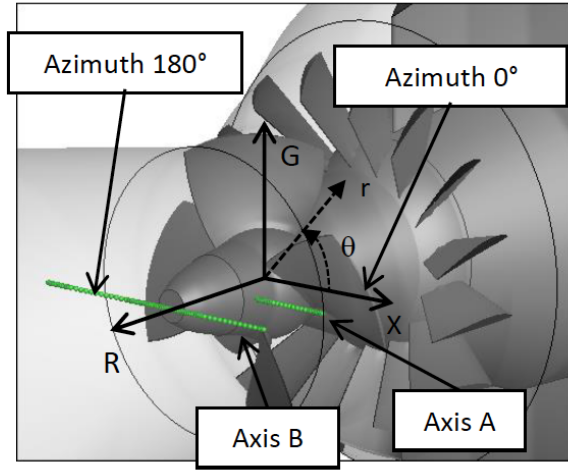
Fig. 16. Location of 4BY0 [31].

Table 2. Relative L^2 norms of difference for pressure profiles.

Scheme	3M	14M	50M
MUSCL	28.72%	9.53%	4.58%
EDDY	21.05%	7.76%	1.66%
EDDY-P	7.50%	7.43%	0.00%

Table 3. Recovery coefficients from the inlet to the outlet.

Scheme	3M	14M	50M
MUSCL	1.0580	0.9194	0.8479
EDDY	0.9906	0.9035	0.8696
EDDY-P	0.9097	0.9074	0.8662

while the EDDY and EDDY-P schemes only slightly under-predicts the peak. It is also notable that as the grid was re-fined, the two side peaks due to the shear flows were captured mildly by the MUSCL scheme and very well by the EDDY schemes on the 14M; while all three schemes resolved the peaks on the 50M grid.

3.3.5 Pressure Profiles

The pressure profiles at 4BY0 are compared in Fig. 26. The numerical result computed by the EDDY-P scheme on the 50M grid is employed as a reference, due to the lack of an experimental distribution of pressure across the cross-section of the draft tube, and denoted by "EDDY-P-50M". The EDDY-P scheme was used as the reference for two rea-sons; first, as the grid is refined, all schemes tend towards the results of the EDDY-P scheme on the 50M grid; and sec-ond, the EDDY-P pressure distribution seems more invari-ant to the grid refinement. The relative L^2 norms of differ-ence against "EDDY-P-50M" for all schemes on all grids are shown in Tab. 2.

Since the swirl flow is weak in the central region in the experiment, according to the steady incompressible momen-tum equations, the gradient of the pressure is also expected to be small. However, on the 3M grid, all three schemes pro-duce large incorrect peaks in the pressure profile. This is due to the mispredicted gradients of the circumferential velocity near the central region in Fig. 20(a). It can be explained al-ternatively by the overprediction of the vorticity magnitude in Fig. 25(a), since the minimum pressure is usually lower in a stronger forced vortex. On the 14M grid, the incor-rect peaks of EDDY and EDDY-P are almost removed, and the prediction by the MUSCL scheme has improved. More-over, compared to the prediction by EDDY, the prediction of EDDY-P is closer to the reference profile EDDY-P-50M, which demonstrates that the dissipation of the scheme is fur-ther reduced. On the 50M grid, the peak for MUSCL contin-ues to diminish, and the predictions of EDDY and EDDY-P are almost equivalent. In summary, the EDDY and EDDY-P

schemes produced better pressure profiles than the MUSCL scheme, and the EDDY-P is less dissipative than EDDY as expected.

3.3.6 Recovery Coefficient

The recovery coefficient is selected as a global quantity for evaluating the overall performance of the draft tube in converting dynamic pressure into static pressure. A general-ized definition of the recovery coefficient is given by [33]:

$$\chi = \frac{p_{outlet} - p_{inlet}}{q} \tag{27}$$

$$= \frac{\frac{\rho}{\dot{m}} \int_{S_{outlet}} p\mathbf{v} \cdot \vec{n} dS - \frac{\rho}{\dot{m}} \int_{S_{inlet}} p\mathbf{v} \cdot \vec{n} dS}{\frac{1}{2S_{inlet}} \rho \int_{S_{inlet}} \mathbf{v} \cdot \mathbf{v} dS}, \tag{28}$$

where q, $\dot{m}$ and S are the dynamic pressure, mass flow rate, and cross-sectional area respectively. The recovery coeffi-cients from the inlet to the outlet are given in Tab. 3. It is observed that the computed recovery coefficients are gener-ally higher on coarser grids. On the 14M and 50M grids, re-covery coefficients computed by all three schemes are quite close to each other. This reveals that for OPs near the BEP, where strong pressure fluctuation does not exist, the MUSCL scheme is able to provide similar prediction on the overall re-covery coefficients compared to the less dissipative schemes EDDY and EDDY-P on moderately fine grids, even if the MUSCL scheme fails in predicting some regional velocity profiles.

4 Conclusions

The eddy-preserving limiter scheme has been extended by employing a new limiting algorithm for the interpolation of pressure. The conventional van Albada limiter is inac-tivated in the interpolation of pressure at smooth extrema. Numerical simulations of three dimensional vortex advection

and the BulbT test cases were performed. Based on the comparisons, it is concluded that the original and extended eddy-preserving limiter schemes are less dissipative and capable of producing better predictions than the baseline MUSCL scheme, and the extended eddy-preserving limiter scheme has slightly improved over the original eddy-preserving limiter scheme.
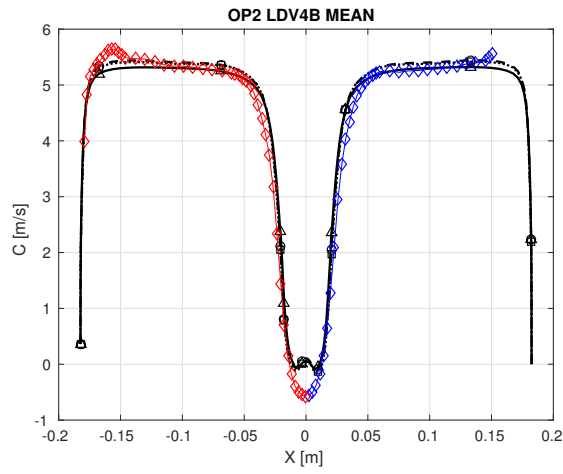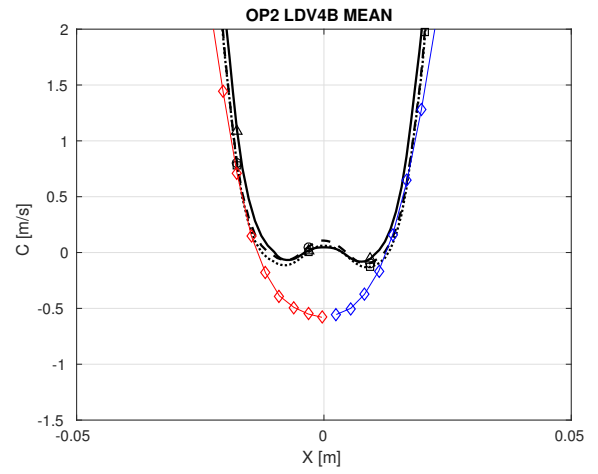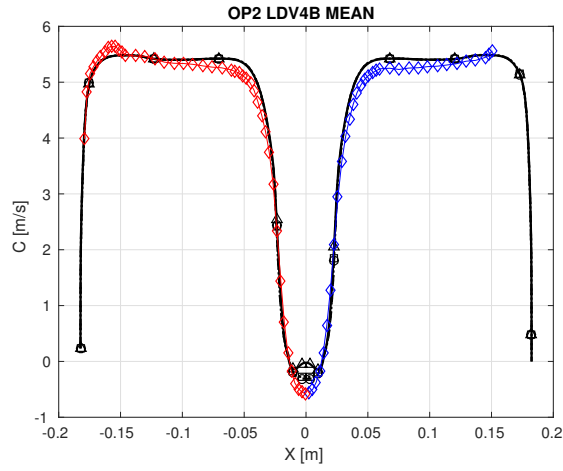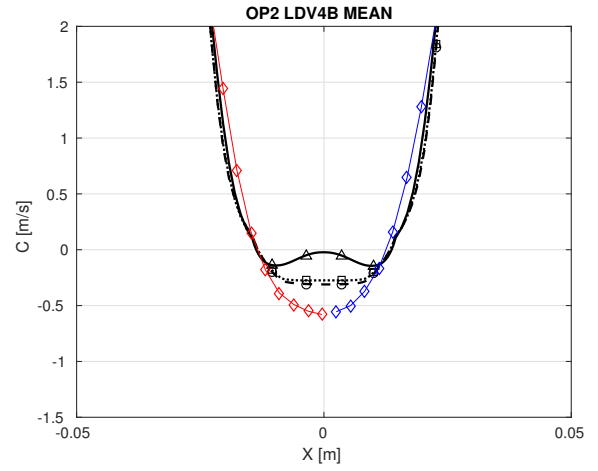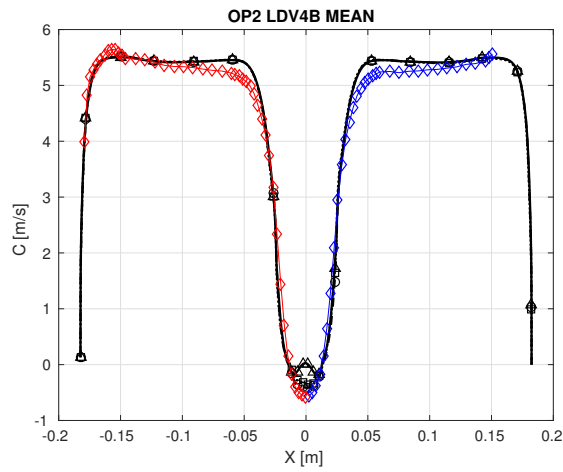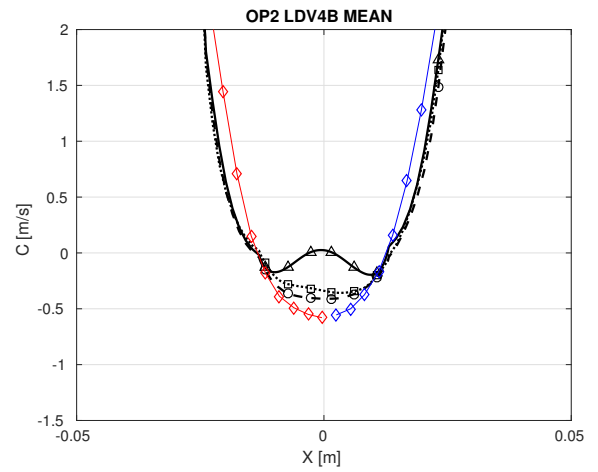
Fig. 17. Axial velocity profiles at 4BY0 on (a)3M (b)14M (c)50M grid. (MUSCL: △; EDDY: ··□··; EDDY-P: ⊖; EXP Cz Az0: ◇; EXP Cz Az180: ◇.)

Fig. 18. Zoom-in view of axial velocity profiles at 4BY0 on (a)3M (b)14M (c)50M grid. (MUSCL: △; EDDY: ··□··; EDDY-P: ⊖; EXP Cz Az0: ◇; EXP Cz Az180: ◇.)
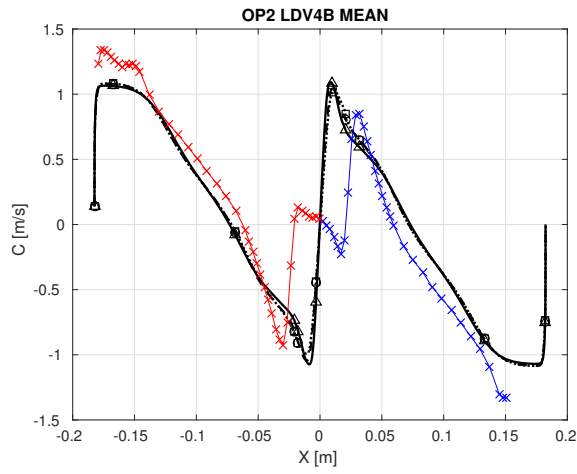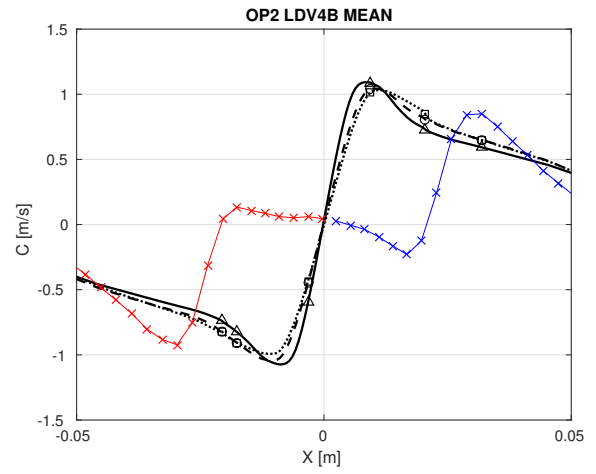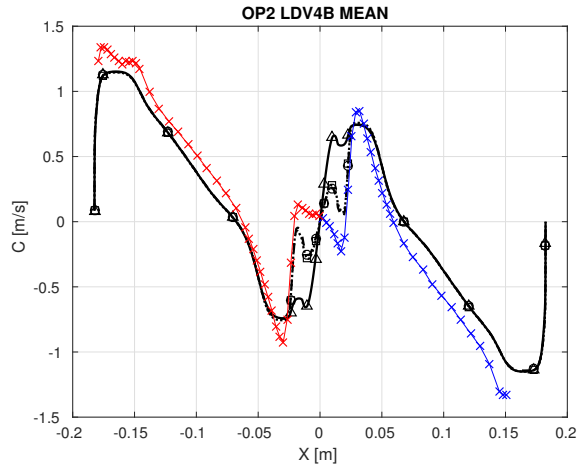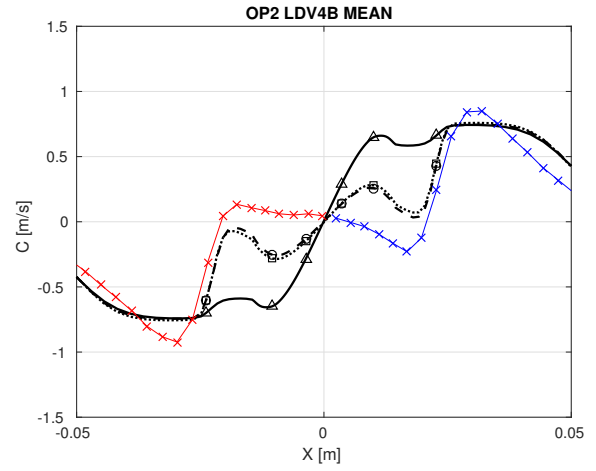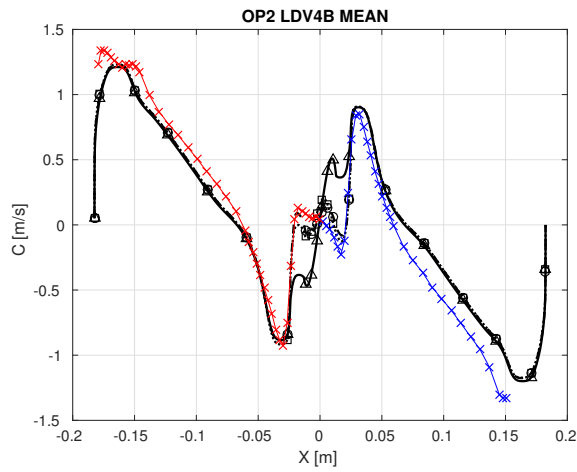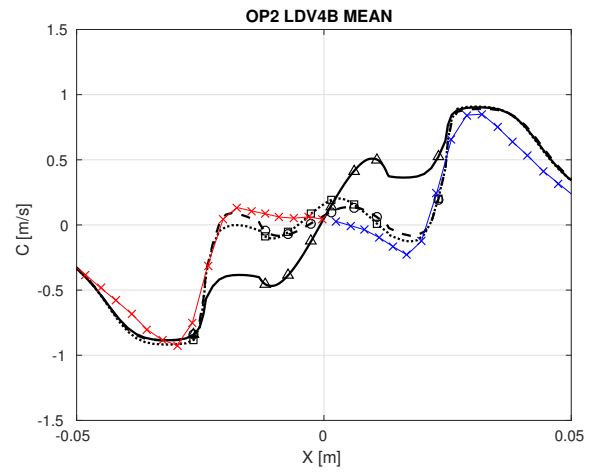
Fig. 19. Circumferential velocity profiles at 4BY0 on (a)3M (b)14M (c)50M grid. (MUSCL: —△—; EDDY: ··□··; EDDY-P: —⊖— ; EXP Cy Az0: —✕—; EXP Cy Az180: —✕—.)

Fig. 20. Zoom-in view of circumferential velocity profiles at 4BY0 on (a)3M (b)14M (c)50M grid. (MUSCL: —△—; EDDY: ··□··; EDDY-P: —⊖— ; EXP Cy Az0: —✕—; EXP Cy Az180: —✕—.)
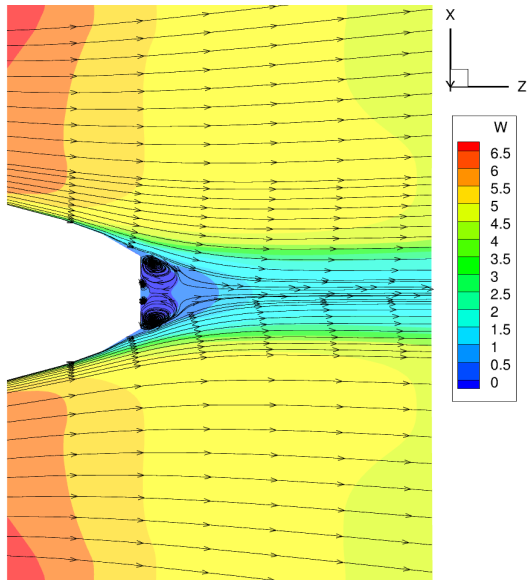
(a)
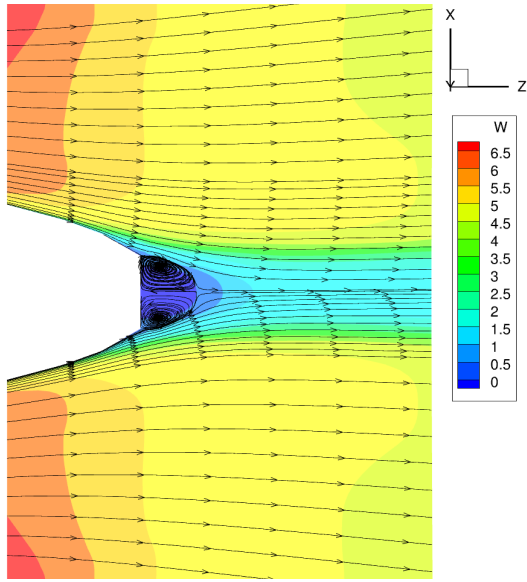
(b)
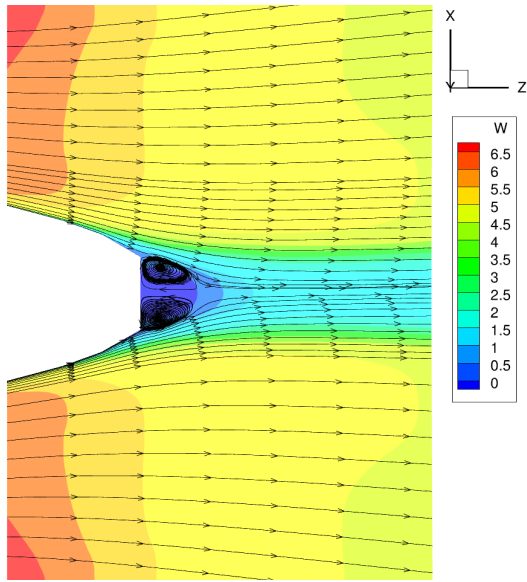
(c)

Fig. 21. Contours of axial velocity and two dimensional streamlines on 14M grid computed by (a)MUSCL (b)EDDY (c)EDDY-P scheme.
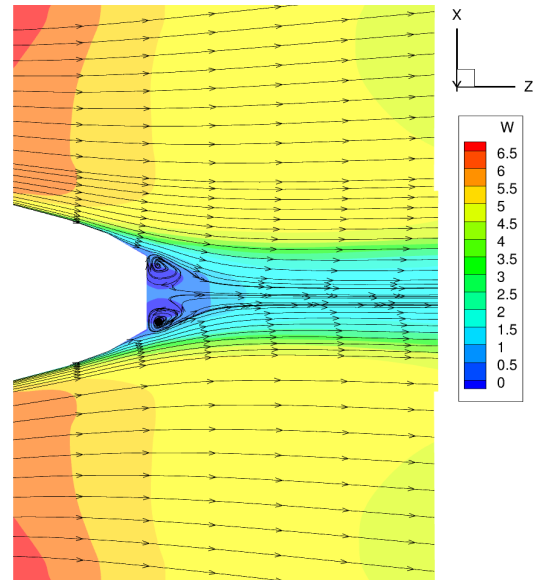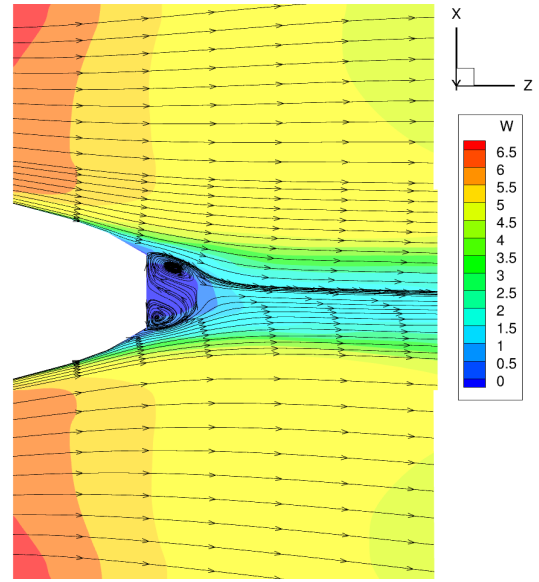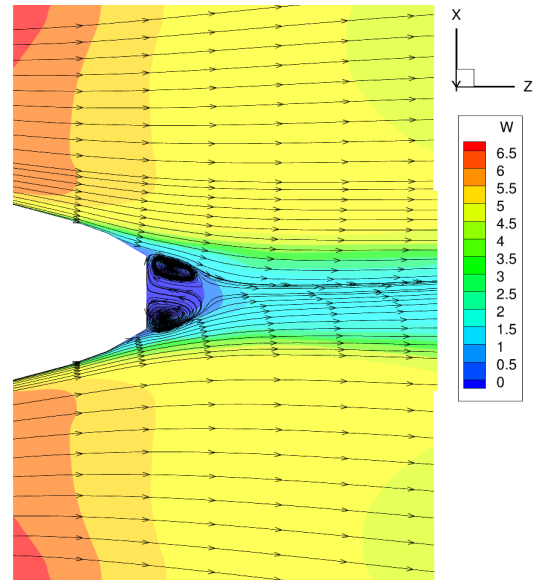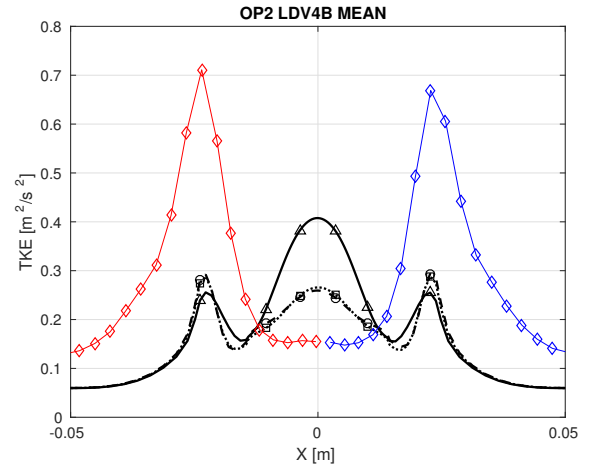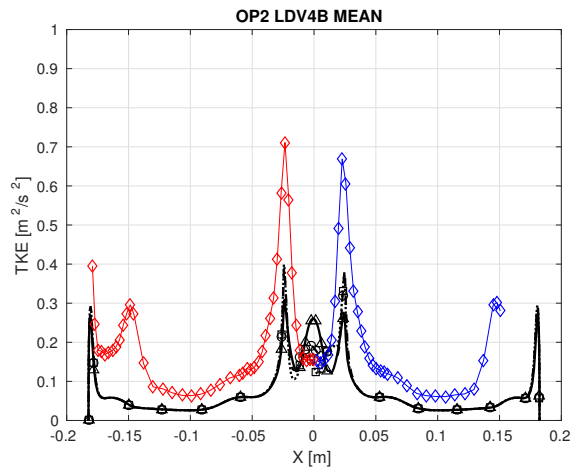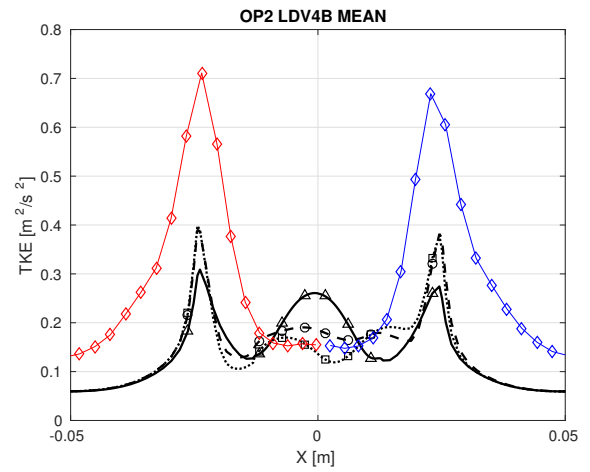
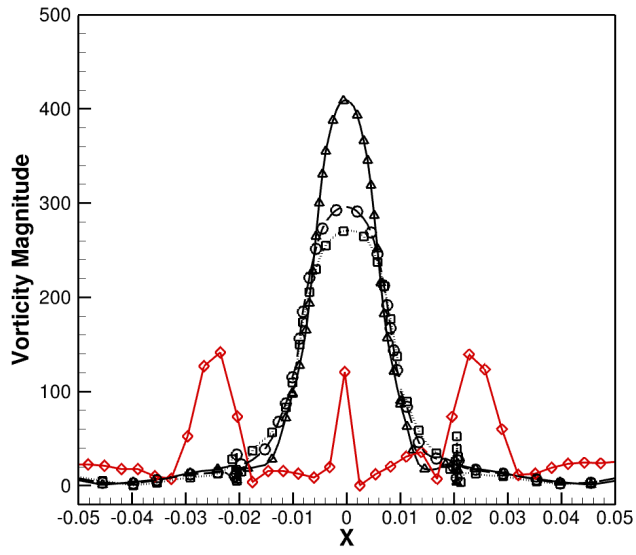Fig. 22. Contours of axial velocity and two dimensional streamlines on 50M grid computed by (a)MUSCL (b)EDDY (c)EDDY-P scheme.
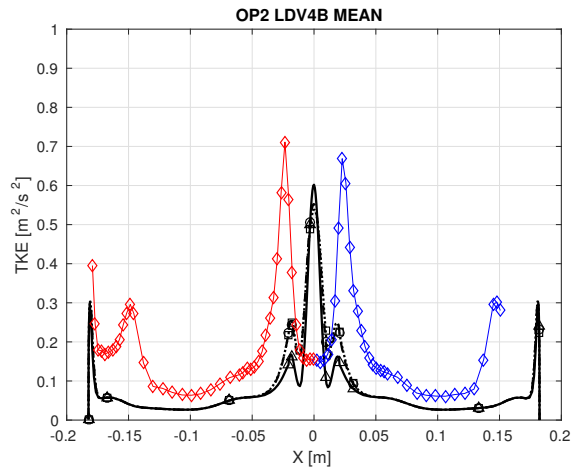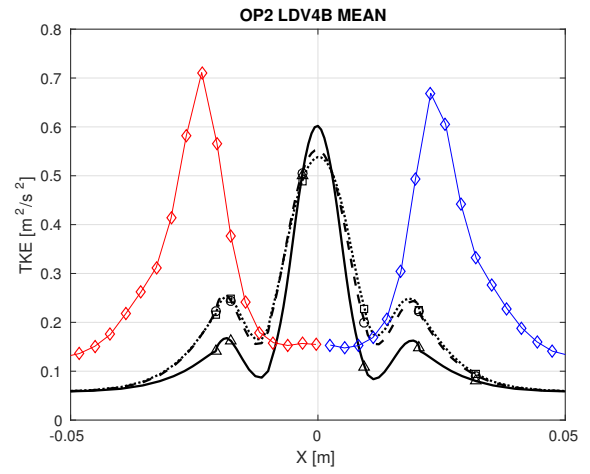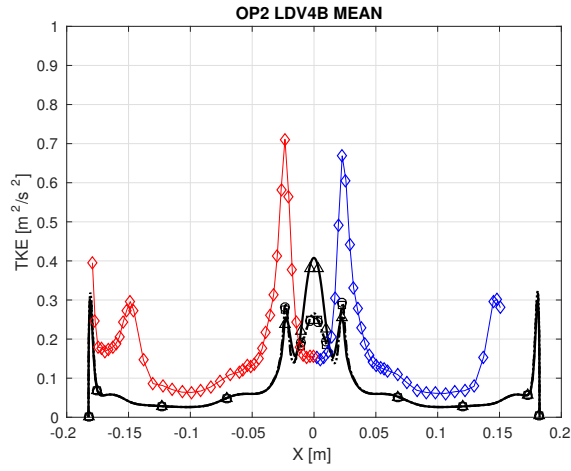
Fig. 23. TKE profiles at 4BY0 on (a)3M (b)14M (c)50M grid. (MUSCL: △; EDDY: ··□··; EDDY-P: -⊖-; EXP TKE Az0: ◇; EXP TKE Az180: ◇.)

Fig. 24. Zoom-in view of TKE profiles at 4BY0 on (a)3M (b)14M (c)50M grid. (MUSCL: △; EDDY: ··□··; EDDY-P: -⊖-; EXP TKE Az0: ◇; EXP TKE Az180: ◇.)
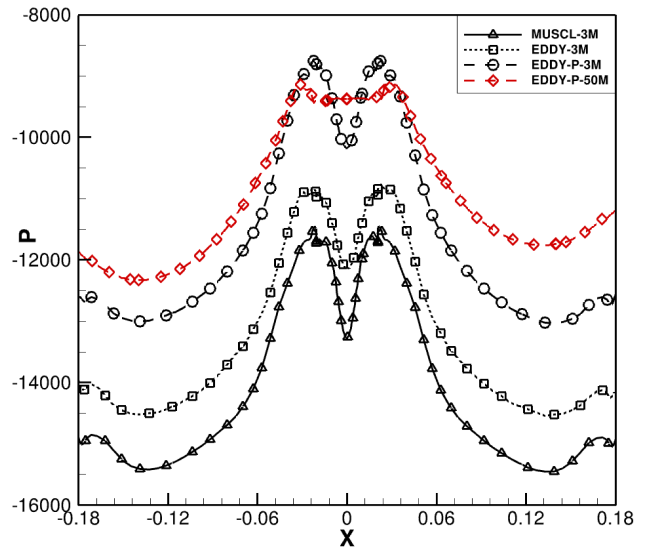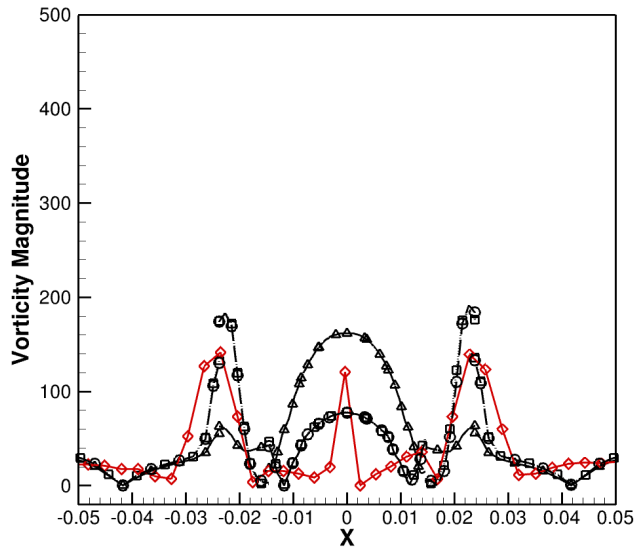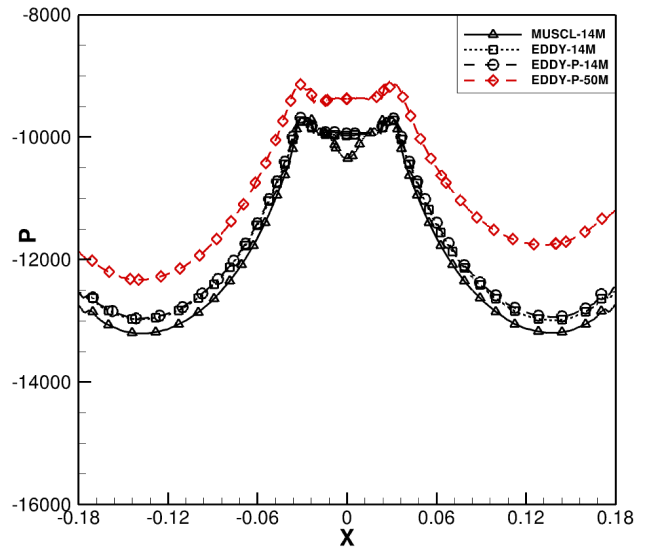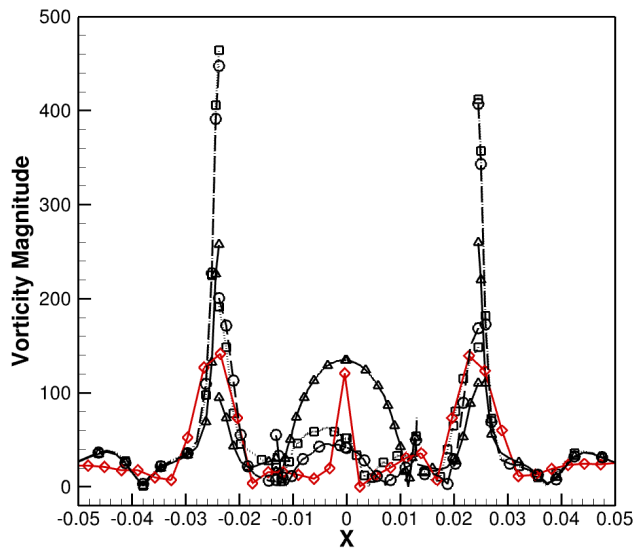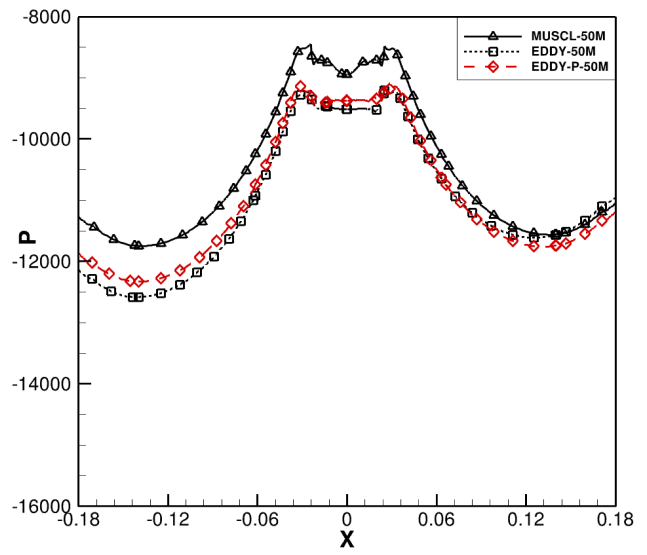
Fig. 25. Vorticity magnitude at 4BY0 on (a)3M (b)14M (c)50M grid.
(MUSCL: ─△─; EDDY: ··□··; EDDY-P: ─○─ ; EXP: ─◇─.)

Fig. 26. Pressure profiles at 4BY0 on (a)3M (b)14M (c)50M grid.

References

[1] Sick, M., Doerfler, P., Sallaberger, M., Lohmberg, A., and Casey, M., 2002. "Cfd simulation of the draft tube vortex". In Proc. 21st IAHR Symp. Hydraulic Machinery & Systems, Lausanne, Switzerland, Paper, no. 32, pp. 1–9.

[2] Dörfler, P., Sick, M., and Coutu, A., 2012. *Flow-induced pulsation and vibration in hydroelectric machinery: engineers guidebook for planning, design and troubleshooting*. Springer Science & Business Media.

[3] Ruprecht, A., Helmrich, T., Aschenbrenner, T., and Scherer, T., 2002. "Simulation of vortex rope in a turbine draft tube". In Proceedings of 22nd IAHR Symposium on Hydraulic Machinery and Systems, pp. 9–12.

[4] Stein, P., Sick, M., Dörfler, P., White, P., and Braune, A., 2006. "Numerical simulation of the cavitating draft tube vortex in a francis turbine". In Proceedings of the 23rd IAHR Symposium on Hydraulic Machinery and Systems, Yokohama, Japan, p. 228.

[5] Jošt, D., and Lipej, A., 2009. "Numerical prediction of the vortex rope in the draft tube". In Proceedings of the 3rd IAHR International Meeting of the Workgroup on Cavitation and Dynamic Problems in Hydraulic Machinery and Systems, pp. 75–85.

[6] Jošt, D., and Lipej, A., 2011. "Numerical prediction of non-cavitating and cavitating vortex rope in a francis turbine draft tube". *Strojniški vestnik-Journal of Mechanical Engineering, 57*(6), pp. 445–456.

[7] Foroutan, H., and Yavuzkurt, S., 2012. "Simulation of flow in a simplified draft tube: turbulence closure considerations". In IOP Conference Series: Earth and Environmental Science, Vol. 15, IOP Publishing, p. 022020.

[8] Foroutan, H., and Yavuzkurt, S., 2014. "Flow in the simplified draft tube of a francis turbine operating at partial loadpart i: Simulation of the vortex rope". *Journal of Applied Mechanics, 81*(6), p. 061010.

[9] Krappel, T., Ruprecht, A., Riedelbauch, S., Jester-Zuerker, R., and Jung, A., 2014. "Investigation of francis turbine part load instabilities using flow simulations with a hybrid rans-les turbulence model". In IOP Conference Series: Earth and Environmental Science, Vol. 22, IOP Publishing, p. 032001.

[10] Chen, X., 1995. "Multi-dimensional finite volume simulation of fluid flows on fixed, moving and deforming mesh systems".

[11] Skotak, A., 2000. "Of the helical vortex in the draft tube turbine modeling". In IAHR Symposium, Charlotte.

[12] Guo, Y., Kato, C., and Miyagawa, K., 2006. "Large-eddy simulation of non-cavitating and cavitating flows in the draft tube of a francis turbine". In Proceedings of the 23rd IAHR Symposium on Hydraulic Machinery and Systems, Yokohama, Japan, p. 95.

[13] Magnan, R., Cupillard, S., Gauthier, G., Giroux, A., Page, M., et al., 2014. "Challenges in assessing the grid sensitivity of hydro-turbine cfd simulations". In IOP Conference Series: Earth and Environmental Science, Vol. 22, IOP Publishing, p. 022010.

[14] Venkatakrishnan, V., 1993. "On the accuracy of limiters and convergence to steady state solutions". *AIAA Paper*(93-0880).

[15] Huynh, H. T., 1995. "Accurate upwind methods for the euler equations". *SIAM Journal on Numerical Analysis, 32*(5), pp. 1565–1619.

[16] Sekora, M., and Colella, P., 2009. "Extremum-preserving limiters for muscl and ppm". *arXiv preprint arXiv:0903.4200*.

[17] Löhner, R., 2009. "On limiters for minimal vorticity dissipation". In Proceedings of the 47th AIAA aerospace sciences meeting, pp. 1–7.

[18] Mohamed, K., Nadarajah, S., and Paraschivoiu, M., 2012. "Eddy-preserving limiter for unsteady subsonic flows". *AIAA Journal, 50*(2), pp. 429–446.

[19] Chakraborty, P., Balachandar, S., and Adrian, R. J., 2005. "On the relationships between local vortex identification schemes". *Journal of Fluid Mechanics, 535*, pp. 189–214.

[20] Vu, T., Gauthier, M., Nennemann, B., Wallimann, H., and Deschênes, C., 2014. "Cfd analysis of a bulb turbine and validation with measurements from the bulbt project". In IOP Conference Series: Earth and Environmental Science, Vol. 22, IOP Publishing, p. 022008.

[21] Goncalves, E., and Patella, R. F., 2009. "Numerical simulation of cavitating flows with homogeneous models". *Computers & Fluids, 38*(9), pp. 1682–1696.

[22] Chang, C.-H., and Liou, M.-S., 2007. "A robust and accurate approach to computing compressible multiphase flow: Stratified flow model and ausm+-up scheme". *Journal of Computational Physics, 225*(1), pp. 840–873.

[23] Le Métayer, O., Massoni, J., and Saurel, R., 2004. "Élaboration des lois d'état d'un liquide et de sa vapeur pour les modčles d'écoulements diphasiques". *International journal of thermal sciences, 43*(3), pp. 265–276.

[24] Paillere, H., Corre, C., and Cascales, J. G., 2003. "On the extension of the ausm+ scheme to compressible two-fluid models". *Computers & Fluids, 32*(6), pp. 891–916.

[25] Barberon, T., and Helluy, P., 2005. "Finite volume simulation of cavitating flows". *Computers & Fluids, 34*(7), pp. 832–858.

[26] Saurel, R., and Abgrall, R., 1999. "A simple method for compressible multifluid flows". *SIAM Journal on Scientific Computing, 21*(3), pp. 1115–1145.

[27] Shyue, K.-M., 1999. "A fluid-mixture type algorithm for compressible multicomponent flow with van der waals equation of state". *Journal of Computational Physics, 156*(1), pp. 43–88.

[28] Luo, H., Baum, J. D., and Löhner, R., 2004. "On the computation of multi-material flows using ale formulation". *Journal of Computational Physics, 194*(1), pp. 304–328.

[29] Gallouët, T., Hérard, J.-M., and Seguin, N., 2002. "Some recent finite volume schemes to compute euler equations using real gas eos". *International Journal for Numerical Methods in Fluids, 39*(12), pp. 1073–1138.

[30] Turkel, E., 1987. "Preconditioned methods for solving the incompressible and low speed compressible equations". *Journal of Computational Physics,* **72**(2), pp. 277–298.

[31] Vuillemard, J., Aeschlimann, V., Fraser, R., Lemay, S., and Deschênes, C., 2014. "Experimental investigation of the draft tube inlet flow of a bulb turbine". In IOP Conference Series: Earth and Environmental Science, Vol. 22, IOP Publishing, p. 032010.

[32] Pereira, M., Duquesne, P., Aeschlimann, V., and Deschênes, C., 2017. "Flow field investigation in a bulb turbine diffuser". In Journal of Physics: Conference Series, Vol. 813, IOP Publishing, p. 012047.

[33] Fox, R., and McDonald, A., 1971. "Effects of swirling inlet flow on pressure recovery in conical diffusers". *AIAA Journal,* **9**(10), pp. 2014–2018.